PCCP

RSC Publishing

PAPER

View Article Online
View Journal | View Issue

Cite this: *Phys. Chem. Chem. Phys.*, 2013, **15**, 10978

Understanding the effect of surface/bulk defects on the photocatalytic activity of TiO_2: anatase *versus* rutile†

Junqing Yan,[a] Guangjun Wu,[a] Naijia Guan,[a] Landong Li,*[a] Zhuoxin Li[b] and Xingzhong Cao[b]

Received 1st March 2013,
Accepted 2nd May 2013

DOI: 10.1039/c3cp50927c

www.rsc.org/pccp

The sole effect of surface/bulk defects of TiO_2 samples on their photocatalytic activity was investigated. Nano-sized anatase and rutile TiO_2 were prepared by hydrothermal method and their surface/bulk defects were adjusted simply by calcination at different temperatures, *i.e.* 400–700 °C. High temperature calcinations induced the growth of crystalline sizes and a decrease in the surface areas, while the crystalline phase and the exposed facets were kept unchanged during calcination, as indicated by the characterization results from XRD, Raman, nitrogen adsorption–desorption, TEM and UV-Vis spectra. The existence of surface/bulk defects in calcined TiO_2 samples was confirmed by photoluminescence and XPS spectra, and the surface/bulk defect ratio was quantitatively analyzed according to positron annihilation results. The photocatalytic activity of calcined TiO_2 samples was evaluated in the photocatalytic reforming of methanol and the photocatalytic oxidation of α-phenethyl alcohol. Based on the characterization and catalytic results, a direct correlation between the surface specific photocatalytic activity and the surface/bulk defect density ratio could be drawn for both anatase TiO_2 and rutile TiO_2. The surface defects of TiO_2, *i.e.* oxygen vacancy clusters, could promote the separation of electron–hole pairs under irradiation, and therefore, enhance the activity during photocatalytic reaction.

1. Introduction

Since the discovery of water photolysis on a TiO_2 photoanode by Fujishima and Honda in 1972,[1] semiconductor photocatalysis has attracted significant attention due to its promising application in environment remediation and solar energy conversion.[2–11] Semiconductor materials are the most important issue in heterogeneous photocatalysis research and a variety of materials have been developed as possible photocatalysts so far.[5,8] Among all the semiconductor materials investigated, TiO_2 is regarded as a benchmark photocatalyst under ultraviolet irradiation because of its superior photocatalytic activity, good chemical stability and high resistance to photocorrosion. Extensive research has been carried out on the application of TiO_2 as a photocatalyst in various reactions and distinctly different photocatalytic properties have been reported.[9–11] It is generally acknowledged that the photocatalytic performance of TiO_2 samples can be greatly influenced by their physico-chemical properties, especially crystalline phases, exposed crystal facets and surface/bulk defects. However, a direct correlation of the physico-chemical properties with photocatalytic performance is rather difficult and conflicting results can always be seen.

The crystalline phase of TiO_2 is one of the most important factors influencing its photocatalytic performance. Anatase and rutile TiO_2, both with tetragonal structure, are most commonly used in photocatalytic reactions. In early studies, anatase TiO_2 was believed to be a more efficient photocatalyst than rutile TiO_2 due to its higher Fermi level and higher degree of hydroxylation.[9] For example, Verykios and Karakitsou report that the photocatalytic hydrogen production from water splitting over platinized TiO_2 is significantly affected by the crystalline structure of TiO_2 and anatase phase exhibits a higher hydrogen

[a] *Key Laboratory of Advanced Energy Materials Chemistry (Ministry of Education), College of Chemistry, Nankai University, Tianjin 300071, P.R. China. E-mail: lild@nankai.edu.cn; Fax: +86-22-23500341; Tel: +86-22-23500341*

[b] *Key Laboratory of Nuclear Analysis Techniques, Institute of High Energy Physics, Chinese Academy of Sciences, Beijing 100049, P.R. China*

† Electronic supplementary information (ESI) available: experimental setup for the photocatalytic reforming of methanol, structure configuration and Raman vibrational mode analysis of anatase and rutile TiO_2, and more XPS of anatase and rutile TiO_2. See DOI: 10.1039/c3cp50927c

production rate than rutile by several times.[12] Matsumura *et al.* report that rutile TiO_2 has poor activity for the reduction of oxygen, and therefore, shows very low activity in the photocatalytic oxidation of 2-propanol using oxygen as the electron acceptor.[13] However, rutile TiO_2 has also been claimed to exhibit higher photocatalytic activity than anatase in the decomposition of methylene blue due to its higher crystallinity.[14] In the work of Palmisano *et al.*,[15,16] nano-structured rutile TiO_2 exhibited high photocatalytic activity and high selectivity in the partial oxidation of aromatic alcohols to the corresponding aldehydes in water suspension. Compared to pure phase anatase or rutile, the mixed-phase TiO_2, Degussa P25 as an example, has been proposed to exhibit higher photocatalytic activity. Li *et al.*[17] propose that the photocatalytic activity of TiO_2 is directly related to the surface-phase structure and the phase junction formed between anatase and rutile can enhance the photocatalytic activity for hydrogen production from water splitting.

The exposed facet of TiO_2 crystal is another important factor influencing its photocatalytic performance. The essence of exposed facets is the surface atomic configuration and coordination, which show great effects on the adsorption and reactivity of semiconductor materials.[18] Lu *et al.*[19] demonstrate that the {001} facets of anatase TiO_2 with high-energy are much more reactive than the thermodynamically stable {101} facets for the production of hydrogen from water splitting. However, Majima *et al.*[20] draw a different conclusion based on single-molecule imaging and kinetic analysis results. Cheng *et al.*[21] report that clean {001} facets exhibit lower reactivity than {101} facets in both photooxidation and photoreduction, while the {010} facets show the highest photoreactivity. In the work of Murray *et al.*,[22] platinized {101} facets are proved to be more active than platinized {001} facets for the production of hydrogen from water splitting.

Besides the crystalline phase and exposed crystal facet, the surface/bulk defect on TiO_2 is another very important factor influencing its photocatalytic performance. In fact, the defects on TiO_2 have been extensively characterized by various techniques, and their roles in adsorption and surface reactivity have been well acknowledged.[23–29] Most recently, Li *et al.*[30] report that tuning the relative concentration ratio of bulk defects to surface defects in TiO_2 nanocrystals can improve the separation of photogenerated electron–hole and therefore can enhance photocatalytic efficiency. However, it is still challenging to correlate the surface defects with the photocatalytic activity. A major problem is that the defects are interacting with many other factors and the photocatalytic activity of TiO_2 is dominated by the balance among all these factors. One should bear in mind that defects exist in most TiO_2 samples except perfect single crystals, and the degrees of defects may differ a lot in different samples. Therefore, it is almost impossible to exclude the effects of defects on the photocatalytic activity of TiO_2 when studying the effects from other factors, *e.g.* crystalline phases and exposed crystal facets, while it is rational to investigate the sole effect of defects on the photocatalytic activity of TiO_2, providing that other factors could be kept unchanged.

In the present study, we aim to provide a comprehensive understanding of the effects of surface/bulk defects on the photocatalytic activity of TiO_2. For this purpose, two commonly used TiO_2 phases, *i.e.* anatase and rutile, are prepared and their surface/bulk defects are adjusted simply by calcination at different temperatures. The photocatalytic activity of TiO_2 samples is evaluated in two typical reactions, *i.e.* photocatalytic alcohol oxidation and photocatalytic methanol reforming. With all the other influencing factors strictly restricted, a direct correlation between surface/bulk defect density and photocatalytic activity is drawn, which is of great significance for the design of a photocatalyst with improved performance.

2. Experimental section

2.1 Preparation of TiO_2 samples

All of the chemical reagents (analytical grade) were purchased from Alfa Aesar Chemical Co. and used as received without further purification. Distilled water was used in all experiments. Anatase and Rutile TiO_2 were prepared by hydrothermal method according to previous literature reports.[31] In a typical synthesis of anatase TiO_2, titanium tetrachloride ($TiCl_4$) was dropwise added into ice water under stirring to prepare a $TiCl_4$ aqueous solution with a concentration of *ca.* 1 mol L^{-1}. Then, 30 mL of $TiCl_4$ aqueous solution was mixed with 30 mL of KOH solution (1 mol L^{-1}), and the resulting solution was transferred into a 75 mL Teflon-lined autoclave for static crystallization at 100 °C for 24 h. In a typical synthesis of rutile TiO_2, 10 mL of 1 mol L^{-1} $TiCl_4$ aqueous solution was added to 50 mL water and the resulting solution was directly transferred into a 75 mL Teflon-lined autoclave for static crystallization at 180 °C for 24 h. The resulting precipitates after crystallization were separated from the liquid phase by centrifugation, thoroughly washed with water, dried at 100 °C for 24 h, and then subjected to calcination (also called annealing) in flowing air at different temperatures for 12 h. The final products are denoted as A-*n* or R-*n*, where A or R represents anatase or rutile, respectively, and *n* represents the calcination temperature in °C.

2.2 Characterization of TiO_2 samples

The specific surface areas of samples were determined through N_2 adsorption–desorption isotherms at 77 K collected on a Quantachrome iQ-MP gas adsorption analyzer.

X-ray diffraction (XRD) patterns of the samples were recorded on a Bruker D8 diffractometer with CuKα radiation (λ = 1.5418 Å) from 5–80° with a scan speed of $2\theta = 4^\circ$ min^{-1}.

Transmission electron microscopy (TEM) images of samples were acquired on a Philips Tecnai G^2 20 S-TWIN electron microscope at an acceleration voltage of 200 kV. A few drops of alcohol suspension containing the catalyst sample were placed on a carbon-coated copper grid, followed by evaporation at ambient temperature.

Raman analysis was carried out on a Renishaw InVia Raman spectrometer and spectra were obtained with the green line of an Ar-ion laser (514.53 nm) in micro-Raman configuration.

Diffuse reflectance ultraviolet-visible (UV-Vis) spectra of samples (*ca.* 100 mg) were recorded in air against $BaSO_4$ in the region of 200–700 nm on a Varian Cary 300 UV-Vis spectrophotometer.

X-ray photoelectron spectra (XPS) were recorded on a Kratos Axis Ultra DLD spectrometer with a monochromated Al–Ka X-ray source ($h\nu$ = 1486.6 eV), hybrid (magnetic/electrostatic) optics and a multi-channel plate and delay line detector (DLD). All spectra were recorded by using an aperture slot of 300 × 700 microns, survey spectra were recorded with a pass energy of 160 eV and high-resolution spectra with a pass energy of 40 eV. Accurate binding energies (±0.1 eV) were determined with respect to the position of the adventitious C 1s peak at 284.8 eV.

Photoluminescence (PL) spectra were recorded on a Spex FL201 fluorescence spectrophotometer. The samples of *ca.* 100 mg were dry-pressed into self-supporting wafers and then illuminated by 325 nm He–Cd laser as excitation source at ambient temperature.

Positron annihilation experiments were carried out with a fast-slow coincidence ORTEC system with a time resolution of 187 ps full width at half maximum. The sample powder was pressed into a disk (diameter: 10.0 mm, thickness: 1.0 mm). A 5×10^5 Bq source of ^{22}Na was sandwiched between two identical sample disks. Measure spectra were analyzed by computer program LT9.0 (ref. 32) with source correction to evaluate the lifetime component τ_i and corresponding intensity I_i using the expression

$$N(t) = \sum_{i=1}^{k+1} \frac{I_i}{\tau_i} \exp\left(-\frac{t}{\tau_i}\right).$$

2.3 Photocatalytic reaction

Photocatalytic reforming of methanol (also known as photocatalytic water splitting with methanol as sacrificial agent) was performed in a top-irradiation-type Pyrex reaction cell connected to a closed gas circulation and evacuation system under the irradiation of a Xe lamp (wavelength: 320–780 nm) (Fig. S1, ESI†). In a typical experiment, a catalyst sample of 100 mg was suspended in 100 mL 10% methanol aqueous solution in the reaction cell. After being evacuated for 30 min, the reactor cell was irradiated with the Xe lamp at 200 W under stirring. The gaseous products were analyzed by an on-line gas chromatograph (Varian CP-3800) with thermal conductivity detector.

The photocatalytic oxidation of α-phenylethanol was performed in a double-walled quartz cell cooled by water with a 250 W high-pressure Hg lamp (315–420 nm, main wavelength at 365 nm) as a light source. In each experiment, the catalyst of *ca.* 0.3 g was dispersed in the mixture of benzotrifluoride (solvent) and 0.025 mol α-phenylethanol in the quartz cell under stirring. The suspension was then irradiated from inside with oxygen bubbled in at *ca.* 20 mL min^{-1}. The organic products were analyzed by GC (Shimadzu GC-2010 Plus) and GC-MS (Shimadzu GCMS-QP2010 SE). Meanwhile, an absorption apparatus containing saturated $Ba(OH)_2$ solution was equipped down-stream of the quartz cell to determine the quantity of CO_2 that might form during the reaction.

3. Results

3.1 Spectroscopy characterization results

Generally, TiO_2 is present in three different crystalline structures in nature, *i.e.* tetragonal anatase, orthorhombic brookite and tetragonal rutile. The rutile phase is the most stable structure of TiO_2, while the anatase phase can transform to rutile phase at high temperature, *e.g.* 500–700 °C.[33] In the present study, the as-prepared anatase TiO_2 shows extremely high crystalline phase stability, similar to that observed for Hombikat UV-100 (Sachtleben Chemie GmbH)[34] and anatase nano-particles.[35] The XRD patterns in Fig. 1 reveal that the crystalline structure of anatase can be well preserved, without the appearance of trace rutile phase, even after calcination in flowing air at 700 °C for 12 h. The crystallinity of both anatase and rutile phases distinctly increases with increasing calcination temperature, as indicated by the decreases in the full-width-at-half-maximum of the Bragg peaks in the XRD patterns. Based on the Scherrer equation from the broadening of anatase (101) reflection and rutile (110) reflection, the crystalline sizes of anatase and rutile increase from 12.3 to 25.4 nm and from 22.3 to 45.1 nm, respectively, as the calcination temperature increases from 400 to 700 °C. The increases in the crystallinity and crystalline size are accompanied by distinct decreases in the surface area of samples, as shown in Table 1.

Raman spectroscopy is further employed in the characterization of crystalline structure of TiO_2 samples, and the results are shown in Fig. 2. The anatase structure is characterized by the tetragonal space group of *I*41/*amd* and six Raman transitions ($1A_{1g}$, $2B_{1g}$ and $3E_g$) are allowed according to the factor group analysis. The rutile structure is characterized by the tetragonal space group of *P*42/*mnm* and five Raman transitions (B_{1g}, multi-proton process, E_g, A_{1g} and B_{2g}) are allowed.[36,37] In the present study, four Raman-active modes of E_g (140 cm^{-1}), B_{1g} (395 cm^{-1}), A_{1g} (515 cm^{-1}) and E_g (635 cm^{-1}) are observed for anatase TiO_2 calcined at different temperatures, while three Raman-active modes of multi-proton process (230 cm^{-1}), E_g (445 cm^{-1}) and A_{1g} (610 cm^{-1}) are observed for rutile TiO_2 calcined at different temperatures. It is clearly indicated that both the anatase structure and the rutile structure are well preserved after calcination, which is consistent with XRD patterns.

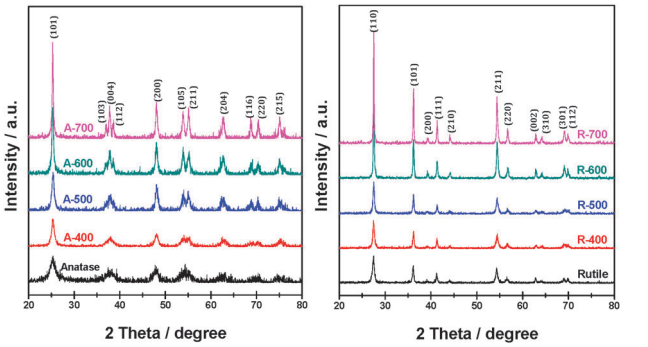

Fig. 1 XRD patterns of anatase and rutile TiO_2 samples calcined at different temperatures.

Table 1 Physico-chemical properties of anatase and rutile TiO_2 samples

Sample	Crystalline structure	Crystallite size (nm) XRD[a]	Crystallite size (nm) TEM[b]	S_{BET} (m^2 g^{-1})
A-400	Anatase	12.3	16.6	142.4
A-500	Anatase	13.6	20.4	69.4
A-600	Anatase	19.4	30.8	38.5
A-700	Anatase	25.4	42.5	20.9
R-400	Rutile	22.3	125.8 × 17.2	24.1
R-500	Rutile	25.5	139.7 × 19.7	19.3
R-600	Rutile	36.1	160.3 × 38.2	11.3
R-700	Rutile	45.1	203.7 × 65.6	6.2

[a] Estimated by the Scherrer equation from the broadening of anatase (101) reflection and rutile (110) reflection in XRD, respectively. [b] Estimated by TEM observations.

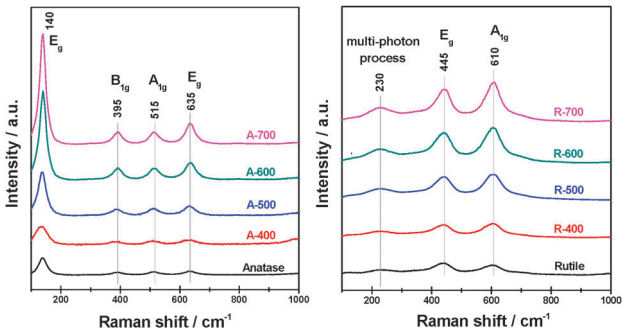

Fig. 2 Raman spectra of anatase and rutile TiO_2 samples calcined at different temperatures.

The intensities and the ratios between different Raman vibrational modes in anatase TiO_2 and rutile are shown in Table S1 and S2 (ESI†), respectively. It is seen that the intensities of Raman vibration modes in both anatase and rutile phase increase as the calcination temperature increases, probably due to the increase in the crystallinity. While the ratios between different Raman vibrational modes, *e.g.* A_{1g}/E_g and B_{1g}/E_g in anatase and A_{1g}/E_g in rutile, are quite similar. It is known that the Raman modes originate from the vibration of molecular bonds and molecular bonds on different crystal facets make different contributions to the Raman-active modes. Raman spectroscopy has been employed in measuring the percentage of specific exposed facets in anatase TiO_2.[29] In the present study, the similar ratios between different Raman vibrational modes indicate that the percentages of specific exposed facets in both anatase and rutile TiO_2 do not change during the calcination process (Fig. S2, Table S1 and S2, ESI† and corresponding discussion).

The morphologies of anatase and rutile TiO_2 samples calcined at different temperatures are investigated by TEM, and the representative TEM images are shown in Fig. 3. The as-prepared anatase TiO_2 appears as aggregates of nano-particles of 2–5 nm. The subsequent calcination process results in an increase in the crystallite size of anatase TiO_2, and larger crystallite sizes are obtained with higher calcination temperatures. The {101} facets are the most thermodynamically stable facets for the regular anatase TiO_2 and these facets account for

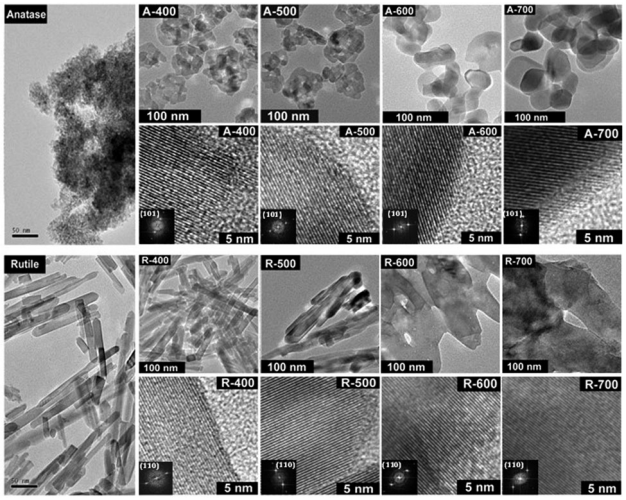

Fig. 3 TEM and HRTEM images of anatase and rutile TiO_2 samples calcined at different temperatures.

the 94% of the total surface according to the Wuff construction.[38] For anatase TiO_2 calcined at different temperatures, the {101} facets are observed as the absolutely dominant facets by the high-resolution transmission electron microscope (HRTEM) images (lattice fringes with spacing of 0.35 nm), further confirmed by fast Fourier transformation (FFT) patterns (Fig. 3). The as-prepared rutile TiO_2 appears as uniform nano-rods, with an average length of 100 nm and diameter of 15 nm. The nano-rods morphology is preserved after calcination at 400 and 500 °C, while the server expansion of nano-rods occurs after calcination at higher temperatures. For all rutile samples, the most stable {110} facets with lowest formation energy[39] are observed as the dominant facets, as illustrated by the lattice fringes with spacing of 0.33 nm in HRTEM images and the corresponding FFT patterns.

For the as-prepared anatase and rutile TiO_2 in the present study, calcination at elevated temperatures can induce the sintering of crystals, which results in an increase in the crystalline size and the decrease in the surface area. However, the crystalline structure as well as the percentage of exposed facets in anatase and rutile TiO_2 is well preserved after calcination at temperatures up to 700 °C, as confirmed by the characterization results from XRD, Raman and TEM. Some physico-chemical properties of the anatase and rutile TiO_2 samples are summarized in Table 1 for a direct view.

Diffuse reflectance UV-Vis spectroscopy was employed to study the optical properties of anatase and rutile TiO_2 samples calcined at different temperatures. All samples show intrinsic absorption in the ultraviolet region attributed to the band–band transition. The calculated band gap of anatase and rutile TiO_2 is 3.2 and 3.0 eV, respectively, consistent with literature results.[40] High temperature calcinations do not change the absorption edges of both anatase and rutile TiO_2, while distinct decreases in the light absorption can be observed. This should be explained from the enhanced scattering of light with larger crystalline size.[41]

Photoluminescence spectroscopy is a very useful technique to disclose the efficiency of charge carrier trapping, immigration and transfer in a semiconductor.[42–45] Generally, the photoluminescence emissions on semiconductor materials are originated from the radiative recombination of photo-generated electrons and holes, and two major photo-physical processes can give rise to photoluminescence signals. When the semiconductor is excited by light with no less than the ban gap energy, the photo-generated electrons can transfer from the conduction band to the valance band, with a release of energy as photoluminescence radiation. This process is recognized as direct band–band transition photoluminescence. In the other photoluminescence process, the excited electrons firstly transfer from the conduction band to different sub-bands, *e.g.* surface oxygen vacancies or defects, *via* non-radiative transition, and subsequently transfer from the sub-bands to the valance band *via* radiative transition with the release of photoluminescence signals. The process is related to the shallow traps and the corresponding photoluminescence signals can be observed in the visible region, considering that the oxygen vacancy or defect states are below the lower end of the conduction band at 0–1 eV.[43] In the present study, the band–band transition photoluminescence signals are observed at 415 and 430 nm for anatase and rutile TiO_2, respectively (Fig. 5). Besides, multiple photoluminescence signals in the visible region (centered at 475 nm) can be observed for both anatase and rutile TiO_2, which are associated with the shallow traps on surface oxygen vacancies or defects. The photoluminescence signals attenuate with increasing calcination temperature for both types of TiO_2, in good agreement with literature reports.[42,46] However, it should be noted that the light absorption also decreases distinctly with increasing calcination temperature, as shown in Fig. 4. Therefore, it is almost impossible to reveal the intrinsic change of photoluminescence signals with calcination temperature. Nevertheless, it can be concluded that abundant surface oxygen vacancies or defects exist in anatase and rutile TiO_2, which may play a vital role in the photocatalytic activity (*vide infra*). Moreover, the relative intensity of surface oxygen vacancies or defects in rutile TiO_2 is higher than that in anatase.

The surface and sub-surface states (at a depth up to 5 nm) of anatase and rutile TiO_2 calcined at different temperatures are investigated by means of XPS and the results are shown in Fig. 6. In the Ti 2p region (Fig. S3, ESI†), binding energy values at 458.3 and 464.1 eV assignable to $2p_{3/2}$ and $2p_{1/2}$ of Ti^{4+} in TiO_2 (ref. 47) are observed for both anatase and rutile calcined at different temperatures, indicating the identical existence state of Ti atoms in these samples. In the O 1s region, binding energy values at 529.6, 531.6 and 533.0 eV are observed in all samples. The binding energy value at 529.6 eV is attributed to crystal lattice oxygen in O–Ti^{4+}, while the binding energy values at 531.6 and 533.0 eV are assigned to surface adsorbed hydroxyl groups.[48–50] Since the physically absorbed hydroxyl groups on TiO_2 can be easily removed under the ultrahigh vacuum condition of the XPS system, TiO_2 single crystal or TiO_2 with fine surface structure will not give significant signals in XPS.[50,51] Therefore, the distinct signals of hydroxyl groups observed should be due to hydroxyl groups, *i.e.* Ti–OH and H_2O, strongly bound to surface defects on anatase and rutile TiO_2 calcined at different temperatures. That is, the hydroxyl groups in XPS are associated with surface defects and the visible hydroxyl groups should indicate the existence of surface defects on TiO_2 samples. As Mul *et al.* reported according to NH_3-TPD experimental results, the number of surface hydroxyl groups per surface area of anatase TiO_2 increases with increasing calcination temperatures.[52] In the present study, a similar trend can be

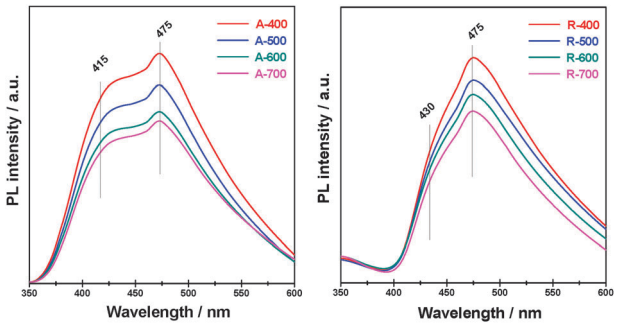

Fig. 5 Photoluminescence spectra of anatase and rutile TiO_2 samples calcined at different temperatures.

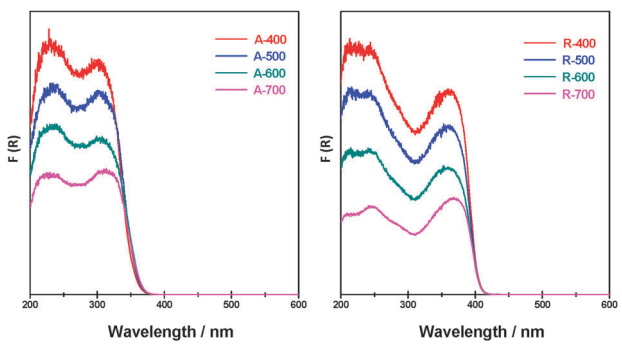

Fig. 4 UV-Vis spectra of anatase and rutile TiO_2 samples calcined at different temperatures.

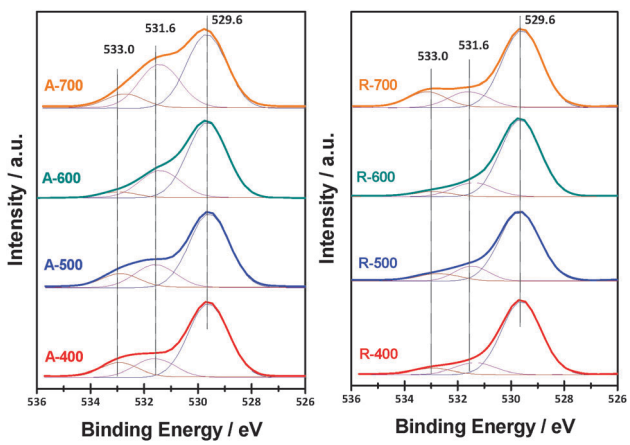

Fig. 6 XPS of the O 1s region of anatase and rutile TiO_2 calcined at different temperatures.

concluded for anatase TiO_2 based on XPS results. However, XPS results are not suitable for the quantitative analysis of surface hydroxyl groups due to the complexity of hydroxyl bound to surface defects as well as the randomness of XPS analysis.

3.2 Characterization of defects by positron annihilation

Positron annihilation is a well-established technique to study the defects in solid materials, and the lifetime of the positron is able to give information on the nature of various defects even at the ppm level.[53–55] In the present study, the defects in different TiO_2 samples are carefully characterized by positron annihilation lifetime spectroscopy. As shown in Table 2, three lifetime components τ_1, τ_2 and τ_3, with relative intensities I_1, I_2, and I_3, are observed for anatase and rutile TiO_2 calcined at different temperatures. The longest component (τ_3) should be attributed to the annihilation of orthopositronium atoms formed in the large voids present in the material[53] and it will not be discussed in the present work. The shortest component τ_1 should be attributed to the free annihilation of positrons in defect-free crystal.[56] In a disordered system, small defects, *e.g.* monovacancies, can reduce the surrounding electron density, and therefore, increase the lifetime of τ_1 (ref. 57). The lifetime τ_1 in anatase and rutile TiO_2 calcined at different temperatures (>200 ps, Table 2) is obviously higher than that of TiO_2 with fine crystal structure ($\sim$180 ps),[58] indicating the existence of small defects in these samples. In this case, τ_1 is the weighted average of free positrons and those trapped by small defects. However, the small defects are not major positron traps and their correlation with material properties is not conclusive.[59] The component τ_2 should be attributed to the annihilation of positrons trapped by large defects, *e.g.* vacancy clusters, in materials. Considering that the average electron density in large defects is lower than that in small defects, the annihilation rates of positrons trapped by large defects are also lower than those trapped by small defects, and therefore, the positrons lifetime is relatively longer.[30] The lifetime component τ_2 qualitatively reveals the nature of large defects and its relative intensity I_2 quantifies the abundance large defects. It has been reported that the deposition of AgI on a TiO_2 surface does not lead to an obvious change of τ_1 but results in a considerable evolution of τ_2.[60] While hydrogenation of TiO_2 results in the distinct increase in τ_1 due to the creation of Ti^{3+}–oxygen vacancies in the bulk phase, with τ_2 nearly unchanged.[29]

Table 2 Positron lifetime and relative intensities of TiO_2 samples

Sample	τ_1 (ps)	I_1 (%)	τ_2 (ps)	I_2 (%)	τ_3 (ns)	I_3 (%)	I_2/I_1	R^a
A-400	200.5	38.92	376.9	58.21	2.219	2.87	1.50	6.6
A-500	207.4	42.90	391.2	54.80	2.274	2.25	1.28	11.5
A-600	219.8	47.90	403.9	48.40	2.225	3.64	1.01	16.4
A-700	213.2	48.20	399.1	47.80	2.291	4.03	0.99	23.6
R-400	208.6	39.60	372.6	56.30	2.071	4.05	1.42	25.4
R-500	201.7	49.83	404.1	48.40	2.032	1.77	0.97	31.5
R-600	212.7	51.10	399.5	46.50	2.186	2.36	0.91	50.3
R-700	214.0	55.30	410.0	42.10	2.137	2.58	0.76	76.6

[a] $R = \frac{C_{surf}}{C_{bulk}} = \frac{I_{surf}/V_{surf}}{I_{bulk}/V_{bulk}} = \frac{I_{surf}/(mS_{BET}\delta_{surf})}{I_{bulk}/(m/\rho_{bulk})} = \frac{I_2}{I_1}\frac{1}{S_{BET}\delta_{surf}\rho_{bulk}}$.

Based on the specific attributions of lifetime components and literature reports, it is rational to propose that the small defects mainly exist in the bulk phase while the large defects mainly locate on the surface or sub-surface of the samples.[29,30,60] For anatase and rutile TiO_2, the lifetime component τ_2 shows considerable variation with calcination temperatures. On the one hand, high-temperature calcinations results in the grain boundary migration and sink of vacancy clusters at original gain surfaces. On the other hand, calcination (thermal energy supply) may induce the migration of sub-surface intra-grain monovacancies to the grain surface and subsequent agglomeration to vacancy clusters. The variations of τ_2 can be explained as a balance of the above-mentioned two conflicting effects. It is interesting to observe that ratios of I_2/I_1 decrease with increasing calcination temperature for both anatase and rutile TiO_2 samples, indicating the loss of vacancy clusters upon calcination. However, it should be noted that the ratio of surface to bulk region in a TiO_2 sample dramatically decreases with increasing crystalline size induced by calcination (Table 1). Here, we introduce the concept of the surface/bulk defects ratio R based on the volume concentration of surface and bulk defects, as shown in the following equation.

$$R = \frac{C_{surf}}{C_{bulk}} = \frac{I_{surf}/V_{surf}}{I_{bulk}/V_{bulk}} = \frac{I_{surf}/(mS_{BET}\delta_{surf})}{I_{bulk}/(m/\rho_{bulk})} = \frac{I_{surf}}{I_{bulk}}\frac{1}{S_{BET}\delta_{surf}\rho_{bulk}} = \frac{I_2}{I_1}\frac{1}{S_{BET}\delta_{surf}\rho_{bulk}}$$

The volume of bulk phase (including the surface layer) is simply calculated as m/ρ_{bulk}, while the volume of the surface layer is calculated as $mS_{BET}\delta_{surf}$, where δ_{surf} is the thickness of the outermost layer of crystalline TiO_2({101} for anatase and {110} for rutile). The calculated R values are listed in Table 2. It is clearly seen that the concentration ratios of surface/bulk defects (R) increase with increasing calcination temperature for both anatase and rutile TiO_2 from 400 to 700 °C, although the intensity ratios of surface/bulk defects show the opposite trend.

3.3 Photocatalytic reaction activities

The photocatalytic activity of anatase and rutile TiO_2 samples calcined at different temperatures is investigated through two typical reactions, *i.e.* photocatalytic reforming of methanol and photocatalytic oxidation of α-phenylethanol.

The time course of hydrogen production from photocatalytic reforming of methanol over anatase and rutile TiO_2 samples calcined at different temperatures (without any co-catalyst) is shown in Fig. 7. It is seen that both anatase and rutile TiO_2 samples exhibit considerable activity for hydrogen production from photocatalytic reforming of methanol. Meanwhile, high-temperature calcinations show distinct effects on the activity. For anatase TiO_2, the mass specific activity decreases slightly with increasing calcination temperature from 400 to 600 °C, reaches to a minimum at 600 °C and then increases with increasing calcination temperature to 700 °C. For rutile TiO_2, the mass specific activity keeps increasing with increasing calcination temperature from 400 to 700 °C. Considering that

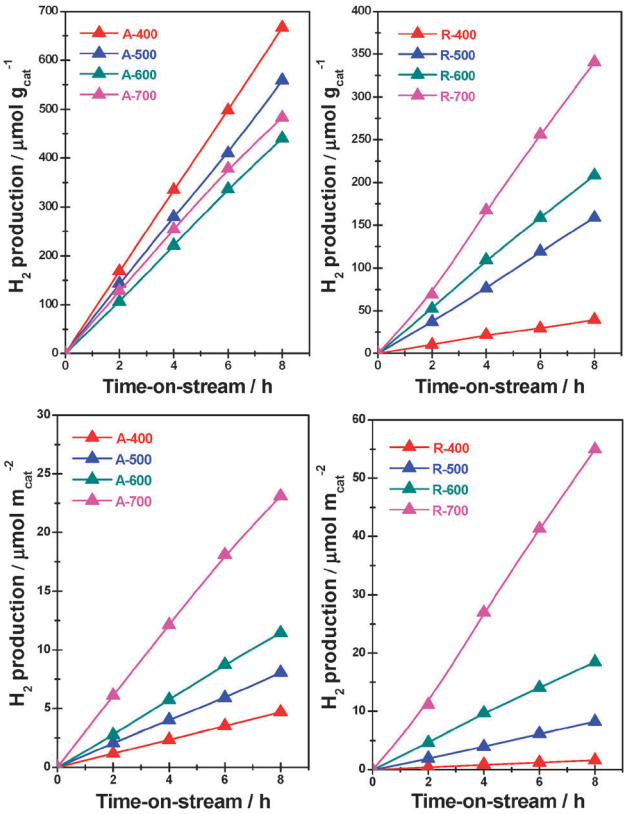

Fig. 7 Hydrogen evolution during methanol photocatalytic reforming over anatase and rutile TiO_2 samples calcined at different temperatures.

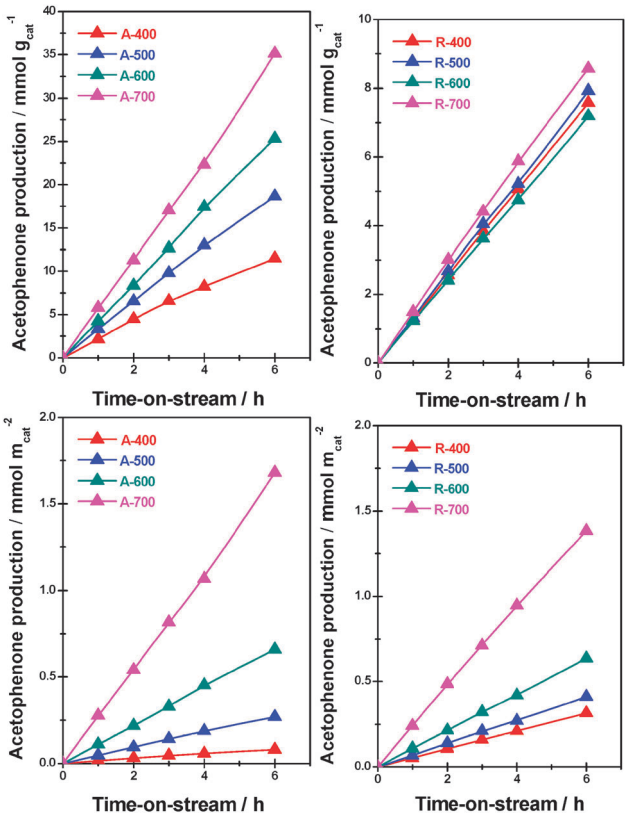

Fig. 8 Acetophenone production during photocatalytic oxidation of α-phenethyl alcohol over anatase and rutile TiO_2 samples calcined at different temperatures.

the surface areas of anatase and rutile TiO_2 samples are very different (Table 1), the surface specific activity (μmol m_{cat}^{-2}) is further calculated to explore the intrinsic photocatalytic activity of TiO_2 samples. As shown in Fig. 7, the surface specific activity of both anatase and rutile increases with increasing calcination temperature from 400 to 700 °C.

The time course of acetophenone production from photocatalytic oxidation of α-phenethyl alcohol over anatase and rutile TiO_2 samples calcined at different temperatures is shown in Fig. 8. The selective photocatalytic oxidation of α-phenethyl alcohol to acetophenane can be achieved on all samples with selectivity of 91–95% (toluene and CO_x as main by-products). For anatase TiO_2, the mass specific activity of α-phenethyl alcohol oxidation keeps increasing with increasing calcination temperature from 400 to 700 °C, while the mass specific activities of α-phenethyl alcohol oxidation on rutile TiO_2 calcined at different temperatures are quite similar. The surface specific activity of both anatase and rutile in the photocatalytic oxidation of α-phenethyl alcohol increases with increasing calcination temperature from 400 to 700 °C, similar to that in the photocatalytic reforming of methanol.

4. Discussion

4.1 Photocatalytic activity: anatase *versus* rutile

The controversies over the activity of anatase and rutile TiO_2 may be originated from many factors and it is difficult to give an exact explanation. In the present study, nano-sized anatase and rutile TiO_2 are prepared without specific shape-control and their activities (without any co-catalyst) are carefully investigated in two typical photocatalytic reactions.

For the photocatalytic reforming of methanol, the activities of both anatase and rutile TiO_2 samples are very much dependent on the calcination temperatures (Fig. 7). In the case of anatase TiO_2, the mass specific activity of the most active sample A-400 (83 μmol h^{-1} g_{cat}^{-1}) is *ca.* 50% higher than that of A-600 (55 μmol h^{-1} g_{cat}^{-1}). In the case of rutile TiO_2, the mass specific activity of the most active sample R-700 (43 μmol h^{-1} g_{cat}^{-1}) is over 8 times higher than that of R-400 (5 μmol h^{-1} g_{cat}^{-1}). Meanwhile, the mass specific activities of anatase TiO_2 in the photocatalytic reforming of methanol are higher than those of rutile TiO_2. However, the surface areas of anatase and rutile TiO_2 samples are quite different (Table 1) and higher surface area may play a positive role in the adsorption of reactant, resulting in higher photocatalytic activity. Thereupon, the surface specific activity (μmol h^{-1} m_{cat}^{-2}) is further calculated to explore the intrinsic photocatalytic activity of TiO_2 samples. The results clearly indicate that comparable surface specific activities in photocatalytic reforming of methanol are obtained on anatase and rutile TiO_2. The highest surface specific activity of 6.8 μmol h^{-1} m_{cat}^{-2} is achieved on rutile sample R-700, in contrast to the surface specific activity of

2.9 μmol h^{-1} m_{cat}^{-2} on anatase sample A-700. More importantly, it should be addressed that the calcination temperatures show significant effects on the surface specific activity of both anatase and rutile TiO_2, and a maximal difference of over 30 times can be observed (6.8 μmol h^{-1} m_{cat}^{-2} for R-700 and 0.2 μmol h^{-1} m_{cat}^{-2} for R-400).

For the photocatalytic oxidation of α-phenethyl alcohol, the circumstances are quite similar to those observed for the photocatalytic reforming of methanol. Anatase TiO_2 samples show a slightly higher mass specific activity than rutile TiO_2 samples, while the surface specific activities of anatase and rutile TiO_2 samples are comparable. Moreover, the product selectivity (to acetophenone) over all TiO_2 samples is quite similar, in great contrast to the reports of Palmisano *et al.*[15,16]

As a whole, it can be concluded that the surface specific activities of anatase and rutile TiO_2 in both photocatalytic reforming of methanol and photocatalytic oxidation of α-phenethyl alcohol are comparable. Calcination temperatures show significant effects on the surface specific activities of anatase and rutile TiO_2. Since the crystalline phase and exposed facets are kept unchanged during the calcination process (Section 3.2), the activity differences between anatase and rutile TiO_2 should originate from the different surface/bulk defects. It should be mentioned that the activity difference originating from different surface/bulk defects (maximal difference of over 30 times) is as least comparable to that originating from the different crystalline phase and exposed facets.[15–22] Fig. 9 shows the direct comparison between the intrinsic photocatalytic activity of home prepared TiO_2 samples (A-700, R-700) and commercial TiO_2 (Hombikat UV-100 with surface area of 288 m^2 g^{-1} and Degussa P25 with surface area of 50 m^2 g^{-1}). It is evident that home prepared pure phase anatase A-700 and rutile R-700 exhibit very good activity in both photocatalytic reforming of methanol and photocatalytic oxidation of α-phenethyl alcohol, using the well-known Degussa P25 as a reference catalyst.

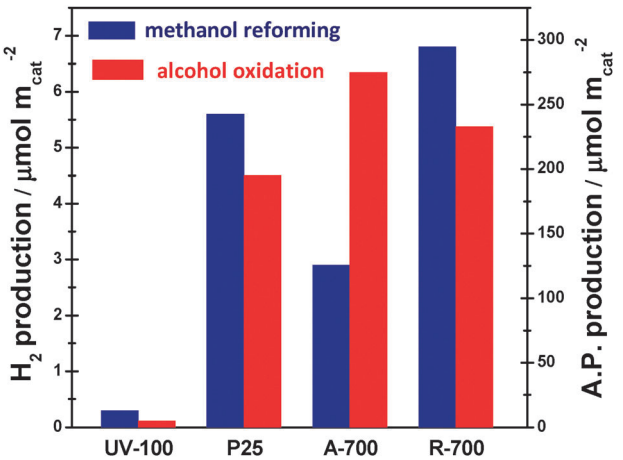

Fig. 9 Surface specific photocatalytic activity of home-prepared A-700 and R-700, and commercial UV-100 and P25.

4.2 Mechanism of photocatalytic reaction

The photocatalytic reaction process on TiO_2 has been extensively investigated, but the detailed mechanism is still unclear. Here, the most simple photocatalytic reaction mechanism will be described by integrating the literature results with our experimental observations.

Under ultraviolet irradiation, electron–hole pairs are created on the surface of TiO_2 (eqn (1)). The photo-generated holes are trapped on the surface defects with low electron density and then react with methanol to produce CO_2 and protons through a series of intermediates (eqn (2)), *e.g.* formaldehyde and formic acid.[61,62] Meanwhile, the photo-generated electrons are trapped on the surface Ti^{4+} sites and lead to the reduction of Ti^{4+} to Ti^{3+} (eqn (3)). The surface-bound Ti^{3+} can reduce protons to adsorbed hydrogen atoms (eqn (4)) and two adjacent hydrogen atoms combine for hydrogen evolution (eqn (5)). In our experiments, all the TiO_2 samples during the photocatalytic reforming of methanol show the blue coloration (Fig. 10), confirming the existence of Ti^{3+} during reaction.[22,63] The visible blue coloration throughout the reaction also indicates that the reduction of protons to hydrogen by Ti^{3+} (eqn (4)) is the rate-determining step for the photocatalytic reforming of methanol. The blue coloration quenches upon exposure to air for *ca.* 30 min in the case of rutile TiO_2 and for *ca.* 5 min in the case of anatase TiO_2.

$$TiO_2 + h\nu \rightarrow TiO_2 + h^+ + e^- \quad (1)$$

$$CH_3OH + H_2O + 6h^+ \xrightarrow{HCHO \rightarrow HCOOH} CO_2 + 6H^+ \quad (2)$$

$$Ti^{4+}(TiO_2)_{surf} + e^- \rightarrow Ti^{3+}(TiO_2)_{surf} \quad (3)$$

$$Ti^{3+}(TiO_2)_{surf} + H^+ \rightarrow Ti^{4+}(TiO_2)_{surf}H_{ad} \quad (4)$$

$$2Ti^{4+}(TiO_2)_{surf}H_{ad} \rightarrow 2Ti^{4+}(TiO_2)_{surf} + H_2 \quad (5)$$

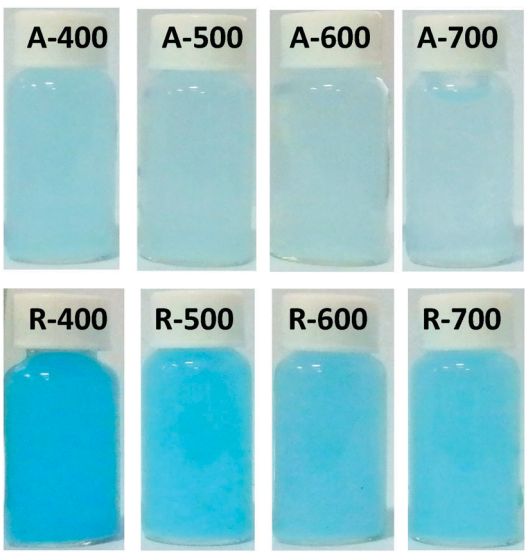

Fig. 10 Photographs of reaction mixtures taken immediately after photocatalytic reforming of methanol.

While for the oxidation of α-phenethyl alcohol, α-phenethyl alcohol first adsorbs onto the surface of TiO_2 and is then oxidized by the photo-generated holes through different radicals as intermediates (eqn (6)).[64,65] Meanwhile, some surface Ti^{4+} sites are reduced to Ti^{3+} by the photo-generated electrons. However, no blue coloration of Ti^{3+} can be observed during the photocatalytic oxidation of α-phenethyl alcohol (using the identical light source as that used in the photocatalytic reforming of methanol), in great contrast to that observed during photocatalytic reforming of methanol. A reasonable explanation is that the Ti^{3+} sites are immediately oxidized to Ti^{4+} by the oxygen in the reaction system (eqn (7)). Therefore, the reaction rate in photocatalytic alcohol oxidation should be much higher than that in photocatalytic alcohol reforming over the same catalyst, as proved by the kinetics data in Fig. 7 and 8.

$$TiO_2 + h\nu \rightarrow TiO_2 + h^+ + e^- \quad (1)$$

$$C_6H_5CH(OH)CH_3 + 2h^+ \xrightarrow{\text{radicals}} C_6H_5COCH_3 + 2H^+ \quad (6)$$

$$Ti^{4+}(TiO_2)_{surf} + e^- \rightarrow Ti^{3+}(TiO_2)_{surf} \quad (3)$$

$$2Ti^{3+}(TiO_2)_{surf} + O_2 + 4H^+ \rightarrow 2Ti^{4+}(TiO_2)_{surf} + 2H_2O \quad (7)$$

Based on the described mechanism of photocatalytic reactions, it is clearly seen that the photocatalytic activity of TiO_2 samples (without any co-catalysts) is only governed by their intrinsic physico-chemical properties. The separation of electron–hole pairs under irradiation should be the direct cause for the different photocatalytic activities of different TiO_2 samples, while the separation of electron–hole pairs on TiO_2 with well-defined crystalline phase and exposed facets is solely dependent on the surface/bulk defects.

4.3 Effect of surface/bulk defects density ratio on photocatalytic activity

As discussed above, many factors, *e.g.* crystalline phase, exposed crystalline facets and surface/bulk defects, may influence the photocatalytic activity of TiO_2. Among these factors, surface/bulk defects have to be considered for most cases except for perfect single crystals. Providing that other factors can be carefully kept unchanged, we are able to study the sole effect of surface/bulk defects on the photocatalytic activity of TiO_2.

Under ultraviolet irradiation with $h\nu \geq E_g$, electrons transfer from valance band to conduction band with the absorption of photo energy and electron–hole pairs are then created on TiO_2. In the case of a TiO_2 crystal free of any defects, the photo-generated electrons and holes undergo quick recombination both in the bulk phase and on the surface. Alternatively, some photo-generated electrons and holes can separately migrate to the surface of TiO_2. The photo-generated electrons on the surface can reduce electron acceptors and the photo-generated holes can oxidize electron donors, initiating the photo-redox reaction. In the case of TiO_2 with surface/bulk defects, the circumstances are a bit more complicated. The photo-generated holes can be trapped by the bulk defects through electrostatic interaction. However, the trapped holes in the bulk phase are not available in photocatalytic reaction and may act as new centers for the recombination with photo-generated electrons (Fig. 11). In another pathway, the photo-generated holes can also be trapped by surface defects, *i.e.* defects clusters, and the separation of photo-generated electron–hole pairs is facilitated. Moreover, the photo-generated holes trapped by surface defects are ready to react with electron donors and the photocatalytic reaction can be greatly promoted. Obviously, the existence of surface defects plays a positive role in the photocatalytic activity of TiO_2 samples. Therefore, it is rational to create more surface defects on TiO_2 samples to enhance their photocatalytic activity. In the present study, a direct correlation between the surface specific photocatalytic activity and surface/bulk defect density ratio R of TiO_2 samples is obtained, as shown in Fig. 12. It is clearly seen that higher specific photocatalytic activity, both in photocatalytic reforming of methanol and photocatalytic alcohol oxidation, is achieved with higher surface/bulk defect density ratio R both in the case of anatase TiO_2 and in the case of rutile TiO_2. It should be mentioned that we could not correlate the surface specific photocatalytic activity with surface/bulk defect density ratio R for TiO_2 samples with different crystal phases, *i.e.* anatase and rutile. Anatase and rutile TiO_2 have different intrinsic properties, *e.g.* Fermi levels and adsorption capabilities to reactants, which show great impacts on their photocatalytic activities. Under these circumstances, it is impossible to study the sole effect of defects on the photocatalytic activity of TiO_2 with different crystal phases.

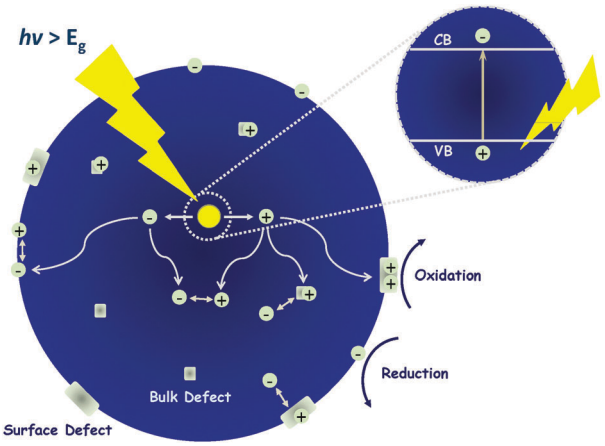

Fig. 11 Recombination pathways of photo-generated electrons and holes on TiO_2 with surface and bulk defects.

Vide supra, the surface/bulk defects show significant effects on the photocatalytic activity of TiO_2, and the effects are more pronounced than, or at least comparable with, those originated from crystalline phase and exposed facets. Since surface/bulk defects exist in most cases, the effects of surface/bulk defects on the photocatalytic activity of TiO_2 samples have to be considered to avoid any possible misunderstanding. It is rational to propose that the controversies over the photocatalytic activity of TiO_2 samples might be related to different degrees of surface/bulk defects. In the present work, positron

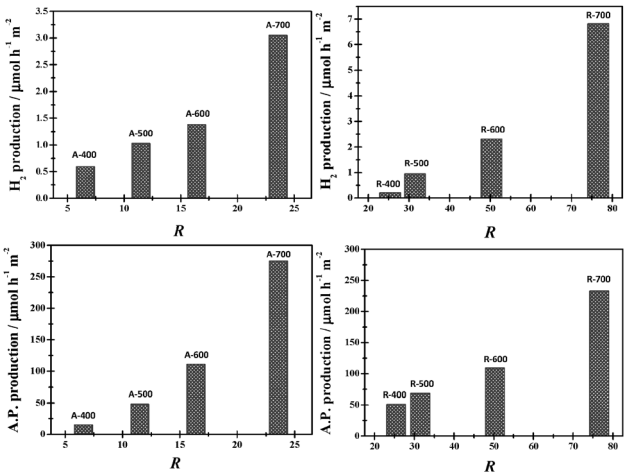

Fig. 12 Correlation between the photocatalytic activities and the surface/bulk defect density ratios R of TiO_2 samples calcined at different temperatures.

annihilation is proved to be a suitable technique to give quantitative information on the surface/bulk defect density ratio, which correlates well with the surface specific activity in photocatalytic reactions.

5. Conclusions

Nano-sized anatase and rutile TiO_2 are prepared by a simple hydrothermal method. Subsequent calcinations of as-prepared TiO_2 samples at 400–700 °C induce the growth of crystalline sizes and the decrease in the surface areas, while the crystalline phase and the exposed facets are kept unchanged during calcination. Characterization results from photoluminescence and XPS spectra indicate the existence of defects in calcined TiO_2 samples. Further results from positron annihilation experiments provide information on the nature and quantitative analysis of surface/bulk defects of TiO_2. It is established that the surface/bulk defect density ratio increases with increasing calcination temperature from 400 to 700 °C both in the case of anatase TiO_2 and in the case of rutile TiO_2.

Calcined anatase and rutile TiO_2 samples are active in the photocatalytic reforming of methanol and the photocatalytic oxidation of α-phenethyl alcohol. The surface specific activities of anatase and rutile TiO_2 in both reactions increase with increasing calcination temperature from 400–700 °C. Since the crystalline phase and the exposed facets are kept unchanged during calcination, the sole effect of surface/bulk defects of anatase and rutile TiO_2 samples on their photocatalytic activity can be investigated. A direct correlation between the surface specific photocatalytic activity and the surface/bulk defect density ratio is drawn for both anatase and rutile TiO_2. The surface/bulk defects can influence the separation of photogenerated electron–hole pairs on TiO_2 under irradiation, and therefore, influence the activity in photocatalytic reaction. Undoubtedly, the effects of surface/bulk defects should NOT be ignored when discussing the photocatalytic activity of TiO_2 or other semiconductor photocatalysis systems.

Acknowledgements

This work is financially supported by the National Basic Research Program of China (2009CB623502) and 111 Project (B12015). Support from the Ministry of Education of China (NCET-11-0251) is also acknowledged.

Notes and references

1 A. Fujishima and K. Honda, *Nature*, 1972, **238**, 37.
2 A. L. Linsebigler, G. Lu and J. T. Yates, *Chem. Rev.*, 1995, **95**, 735.
3 A. M. I. Litter, *Appl. Catal., B*, 1999, **29**, 89.
4 D. Ravelli, D. Dondi, M. Fagnonia and A. Albini, *Chem. Soc. Rev.*, 2009, **38**, 1999.
5 M. D. Hernandez-Alonso, F. Fresno, S. Suarez and J. M. Coronado, *Energy Environ. Sci.*, 2009, **2**, 1231.
6 M. N. Chong, B. Jin, C. W. K. Chow and C. Saint, *Water Res.*, 2010, **44**, 2997.
7 M. A. Henderson, *Surf. Sci. Rep.*, 2011, **66**, 185.
8 H. Tong, S. Ouyang, Y. Bi, N. Umezawa, M. Oshikiri and J. Ye, *Adv. Mater.*, 2012, **24**, 229.
9 O. Carp, C. L. Huisman and A. Reller, *Prog. Solid State Chem.*, 2004, **32**, 33.
10 A. Fujishima, X. Zhang and D. A. Tryk, *Surf. Sci. Rep.*, 2008, **63**, 515.
11 S. G. Kumar and L. G. Devi, *J. Phys. Chem. A*, 2011, **115**, 13211.
12 K. E. Karakitsou and X. E. Verykios, *J. Phys. Chem.*, 1993, **97**, 1184.
13 T. Ohno, K. Sarukawa and M. Matsumura, *J. Phys. Chem. B*, 2001, **105**, 2417.
14 N. Masahashi, Y. Mizukoshi, S. Semboshi and N. Ohtsu, *Appl. Catal., B*, 2009, **90**, 255.
15 S. Yurdakal, G. Palmisano, V. Loddo, V. Augugliaro and L. Palmisano, *J. Am. Chem. Soc.*, 2008, **130**, 1568.
16 S. Yurdakal, G. Palmisano, V. Loddo, O. Alagoz, V. Augugliaro and L. Palmisano, *Green Chem.*, 2009, **11**, 510.
17 J. Zhang, Q. Xu, Z. Feng, M. Li and C. Li, *Angew. Chem., Int. Ed.*, 2008, **47**, 1766.
18 S. Liu, J. Yu and M. Jaroniec, *Chem. Mater.*, 2011, **23**, 4085.
19 H. G. Yang, C. H. Sun, S. Z. Qiao, J. Zou, G. Liu, S. C. Smith, H. M. Cheng and G. Q. Lu, *Nature*, 2008, **453**, 638.
20 T. Tachikawa, S. Yamashita and T. Majima, *J. Am. Chem. Soc.*, 2011, **133**, 7197.
21 J. Pan, G. Liu, G. Q. Lu and H. M. Cheng, *Angew. Chem., Int. Ed.*, 2011, **50**, 2133.
22 T. R. Gordon, M. Cargnello, T. Paik, F. Mangolini, R. T. Weber, P. Fornasiero and C. B. Murray, *J. Am. Chem. Soc.*, 2012, **134**, 6751.
23 Q. Wang, J. Biener, X. C. Guo, E. Farfan-Arribas and R. J. Madix, *J. Phys. Chem. B*, 2003, **107**, 11709.
24 U. Aschauer, Y. He, H. Cheng, S. C. Li, U. Diebold and A. Selloni, *J. Phys. Chem. C*, 2010, **114**, 1278.
25 X. Q. Gong, A. Selloni, M. Batzill and U. Diebold, *Nat. Mater.*, 2006, **5**, 665.

26 E. Lira, S. Wendt, P. Huo, J. Hansen, R. Streber, S. Porsgaard, Y. Wei, R. Bechstein, E. Lægsgaard and F. Besenbacher, *J. Am. Chem. Soc.*, 2011, **133**, 6529.
27 J. Lee, D. C. Sorescu and X. Deng, *J. Am. Chem. Soc.*, 2011, **133**, 10066.
28 A. Naldoni, M. Allieta, S. Santangelo, M. Marelli, F. Fabbri, S. Cappelli, C. L. Bianchi, R. Psaro and V. D. Santo, *J. Am. Chem. Soc.*, 2012, **134**, 7600.
29 X. Jiang, Y. Zhang, J. Jiang, Y. Rong, Y. Wang, Y. Wu and C. Pan, *J. Phys. Chem. C*, 2012, **116**, 22619.
30 M. Kong, Y. Li, X. Chen, T. Tian, P. Fang, F. Zheng and X. Zhao, *J. Am. Chem. Soc.*, 2011, **133**, 16414.
31 H. Cheng, J. Ma, Z. Zhao and L. Qi, *Chem. Mater.*, 1995, **7**, 663.
32 S. Wang, Z. Chen and B. Wang, *Applied Positron Spectroscopy*, Hubei Science and Technology Press, 2008.
33 D. A. H. Hanaor and C. C. Sorrell, *J. Mater. Sci.*, 2011, **46**, 855.
34 Y. Nakaoka and Y. Nosaka, *J. Photochem. Photobiol., A*, 1997, **110**, 299.
35 J. Ye, W. Liu, J. Cai, S. Chen, X. Zhao, H. Zhou and L. Qi, *J. Am. Chem. Soc.*, 2011, **133**, 933.
36 T. Ohsaka, F. Izumi and Y. Fujiki, *J. Raman Spectrosc.*, 1978, **7**, 321.
37 H. L. Ma, J. Y. Yang, Y. Dai, Y. B. Zhang, B. Lu and G. H. Ma, *Appl. Surf. Sci.*, 2007, **253**, 7497.
38 M. Lazzeri, A. Vittadini and A. Selloni, *Phys. Rev. B: Condens. Matter*, 2001, **63**, 155409.
39 V. E. Henrich and A. F. Cox, *The Surface Science of Metal Oxides*, Cambridge University Press, 1993.
40 A. Kudo and Y. Miseki, *Chem. Soc. Rev.*, 2009, **38**, 253.
41 J. G. Yu, H. G. Yu, B. Cheng, X. J. Zhao, J. C. Yu and W. K. Ho, *J. Phys. Chem. B*, 2003, **107**, 13871.
42 L. Jing, Y. Qu, B. Wang, S. Li, B. Jiang, L. Yang, W. Fu, H. Fu and J. Sun, *Sol. Energy Mater. Sol. Cells*, 2006, **90**, 1773.
43 N. Serpone, D. Lawless and R. Khairutdinovt, *J. Phys. Chem.*, 1995, **99**, 16646.
44 Y. Cong, J. Zhang, F. Chen and M. Anpo, *J. Phys. Chem. C*, 2007, **111**, 6976.
45 X. Chen, X. Wang, Y. Hou, J. Huang, L. Wu and X. Fu, *J. Catal.*, 2008, **255**, 59.
46 D. Zhang, J. A. Downing, F. J. Knorr and J. L. McHale, *J. Phys. Chem.*, 2006, **110**, 21890.
47 C. D. Wagner, W. M. Riggs, L. E. Davis, J. F. Moulder and G. E. Muilenberg, *Handbook of X-ray photoelectron spectroscopy: a reference book of standard data for use in x-ray photoelectron spectroscopy*, Perkin-Elmer MN, Eden-Prairie, 1979.
48 G. Pirug, C. Ritke and H. P. Bonzel, *Surf. Sci.*, 1991, **241**, 289.
49 W. Feng, G. Wu, L. Li and N. Guan, *Green Chem.*, 2011, **13**, 3265.
50 A. Iwabuchi, C. Choo and K. Tanaka, *J. Phys. Chem. B*, 2004, **108**, 10863.
51 R. Wang, N. Sakai, A. Fujishima, T. Watanabe and K. Hashimoto, *J. Phys. Chem. B*, 1999, **103**, 2188.
52 J. T. Carneiro, T. J. Savenije, J. A. Moulijn and G. Mul, *J. Phys. Chem. C*, 2010, **114**, 327.
53 R. Krause-Rehberg and H. S. Leipner, *Positron Annihilation in Semiconductors*, Springer, Berlin, 1999.
54 S. Dutta, M. Chakrabarti, S. Chattopadhyay, D. Jana, D. Sanyal and A. Sarkar, *J. Appl. Phys.*, 2005, **95**, 053513.
55 Y. Zhang, X. Ma, P. Chen, D. Li, X. Pi, D. Yang and P. G. Coleman, *Appl. Phys. Lett.*, 2009, **95**, 252102.
56 R. M. de la Cruz, R. Pareja, R. Gonzalez, L. A. Boatner and Y. Chen, *Phys. Rev. B: Condens. Matter*, 1992, **45**, 6581.
57 D. Sanyal, D. Banerjee and U. De, *Phys. Rev. B: Condens. Matter*, 1998, **58**, 15226.
58 H. Murakami, N. Onizuka, J. Sasaki and N. Thonghai, *J. Mater. Sci.*, 1998, **33**, 5811.
59 S. Dutta, S. Chattopadhyay, D. Jana, A. Banerjee, S. Manik, S. K. Pradhan, M. Chakrabarti, M. Sutradhar and A. Sarkar, *Appl. Phys. Lett.*, 2006, **100**, 114328.
60 W. Sun, Y. Li, W. Shi, X. Zhao and P. Fang, *J. Mater. Chem.*, 2011, **21**, 9263.
61 T. Kawai and T. Sakata, *J. Chem. Soc., Chem. Commun.*, 1980, 694.
62 T. Chen, Z. Feng, G. Wu, J. Shi, G. Ma, P. Ying and C. Li, *J. Phys. Chem. C*, 2007, **111**, 8005.
63 T. Torimoto, R. J. Fox III and M. A. Fox, *J. Electrochem. Soc.*, 1996, **143**, 3712.
64 M. Zhang, Q. Wang, C. Chen, L. Zang, W. Ma and J. Zhao, *Angew. Chem., Int. Ed.*, 2009, **48**, 6081.
65 G. Palmisano, E. Garcia-Lopez, G. Marci, V. Loddo, S. Yurdakal, V. Augugliaro and L. Palmisano, *Chem. Commun.*, 2010, **46**, 7074.

